

See discussions, stats, and author profiles for this publication at: <https://www.researchgate.net/publication/51853606>

Acoustically Driven Photon Antibunching in Nanowires

ARTICLE in NANO LETTERS · DECEMBER 2011

Impact Factor: 13.59 · DOI: 10.1021/nl203461m · Source: PubMed

CITATIONS

12

READS

39

13 AUTHORS, INCLUDING:



Michael Möller

University of Valencia

9 PUBLICATIONS 61 CITATIONS

SEE PROFILE



Snezana Lazic

Universidad Autónoma de Madrid

41 PUBLICATIONS 278 CITATIONS

SEE PROFILE



Mauricio M. de Lima, Jr.

University of Valencia

64 PUBLICATIONS 563 CITATIONS

SEE PROFILE



Andres Cantarero

University of Valencia

294 PUBLICATIONS 2,942 CITATIONS

SEE PROFILE

Acoustically Driven Photon Antibunching in Nanowires

A. Hernández-Mínguez,^{*,†} M. Möller,[‡] S. Breuer,[†] C. Pfüller,[†] C. Somaschini,[†] S. Lazić,[†] O. Brandt,[†] A. García-Cristóbal,[‡] M. M. de Lima, Jr.,[‡] A. Cantarero,[‡] L. Geelhaar,[†] H. Riechert,[†] and P. V. Santos[†]

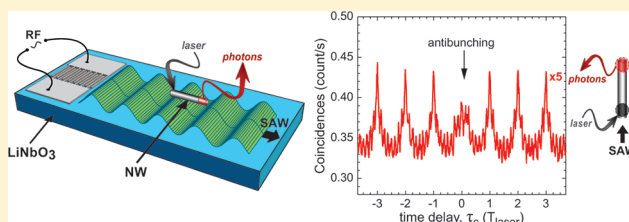
[†]Paul-Drude-Institut für Festkörperelektronik, Hausvogteiplatz 5-7, 10117 Berlin, Germany

[‡]Materials Science Institute, University of Valencia, P.O. Box 22085, ES46071 Valencia, Spain

S Supporting Information

ABSTRACT: The oscillating piezoelectric field of a surface acoustic wave (SAW) is employed to transport photoexcited carriers, as well as to spatially control exciton recombination in GaAs-based nanowires (NWs) on a subns time scale. The experiments are carried out in core-shell NWs transferred to a SAW delay line on a LiNbO₃ crystal. Carriers generated in the NW by a focused laser spot are acoustically transferred to a second location, leading to the remote emission of subns light pulses synchronized with the SAW phase. The dynamics of the carrier transport, investigated using spatially and time-resolved photoluminescence, is well-reproduced by computer simulations. The high-frequency contactless manipulation of carriers by SAWs opens new perspectives for applications of NWs in optoelectronic devices operating at gigahertz frequencies. The potential of this approach is demonstrated by the realization of a high-frequency source of antibunched photons based on the acoustic transport of electrons and holes in (In,Ga)As NWs.

KEYWORDS: Nanowires, surface acoustic waves, acoustic charge transport, photoluminescence, single photon emission



The use of semiconductor nanowires (NWs) offers new possibilities for low-dimensional semiconductor devices.^{1,2} Their small cross-section favors mesoscopic size effects and simultaneously lifts the epitaxial constraints associated with the growth of dissimilar materials, thus opening novel ways for the combination of materials normally impossible in conventional two-dimensional (2D) epitaxial growth. In addition, the geometry of NWs allows for new concepts for opto-electronic devices. Several obstacles need to be overcome for the full exploitation of these favorable features. One of them is associated with the large surface-to-volume ratio, which normally has a deleterious effect on the electronic properties. The second is the need for appropriate techniques for applying electrical control fields, which typically requires doping as well as the contacting of nanometer-sized structures with nonplanar geometry.

In this contribution, we demonstrate that these two obstacles can be surmounted by combining the high quantum efficiency of GaAs/(Al,Ga)As core-shell NWs³ with the remote carrier control by surface acoustic waves (SAWs). SAWs are propagating elastic vibrations confined to the surface of a material. On a piezoelectric semiconductor, these vibrations are accompanied by a piezoelectric potential Φ_{SAW} , which traps electrons and holes in spatially separated positions, thus preventing their recombination while transporting them with the well-defined SAW velocity, v_{SAW} .⁴ SAWs with wavelengths λ_{SAW} in the micrometer range have proven to be a powerful tool to confine and transport free single carriers⁵ as well as spin ensembles^{6–8} in 2D semiconductor heterostructures. The evanescent Φ_{SAW} , which extends to approximately one acoustic

wavelength both below and above the surface, has also been employed for the control of carriers in hybrid systems consisting of a semiconductor structure placed on a piezoelectric substrate. This approach has been used to transport electrically injected carriers in carbon nanotubes^{9–11} and NWs¹² as well as to locally modulate their photoluminescence (PL).^{13,14} We show here that the acoustic fields cannot only remotely control the PL intensity¹⁴ and provide information about the electronic properties of NWs¹⁵ but can also transport photoexcited electrons and holes along the NW axis. In this way, carriers generated on one section of the NW can be transferred to a remote position, where they recombine emitting subnanosecond light pulses. The ambipolar transport over micrometer distances reflects the high opto-electronic quality of the NWs and provides a powerful tool for the contactless control of electronic and photonic excitations in these structures. As an example of a functionality arising from the contactless control of the carrier dynamics, we demonstrate a source of antibunched photons based on the acoustic pumping of emission centers in GaAs NWs capped with an (In,Ga)As segment. These sources combine the high photon extraction efficiency enabled by the NW geometry¹⁶ with the low jitter levels and high repetition arising from the acoustic pumping.¹⁷ The nonclassical nature of this source, which is characterized by a reduced probability of simultaneous emission of multiple photons, has been confirmed by photon

Received: October 4, 2011

Revised: December 1, 2011

Published: December 5, 2011

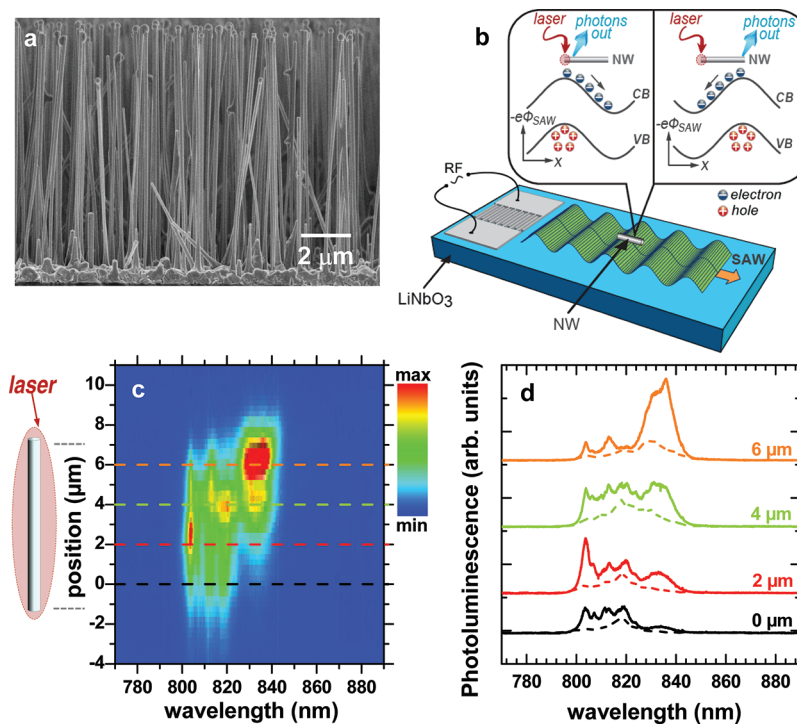


Figure 1. Experimental setup and optical properties of GaAs nanowires (NWs). (a) Scanning electron microscopy side view of as-grown GaAs nanowires on Si. (b) Experimental setup for spectroscopic measurements with the NW lying on the path of a surface acoustic wave (SAW). The SAWs were electrically generated by an interdigitated transducer (IDT) on a LiNbO_3 crystal. The inset shows the modulation of the conduction (CB) and valence band (VB) edges of the NW induced at different phases of the SAW piezoelectric potential Φ_{SAW} (cf. eq 1). (c) Spectrally (horizontal axes) and spatially (vertical axis) resolved photoluminescence of a NW at 20 K excited by an extended laser spot illuminating the whole NW. No SAW was applied in this case. The features in the PL maps are attributed to exciton recombination at centers induced by potential fluctuations along the NW axis (vertical scale). (d) Spectral traces determined at the positions indicated by the dashed lines in (c) in the absence (solid curves) and presence (dashed curves, scaled by a factor of 5) of a SAW excited by an rf power of 3 dBm.

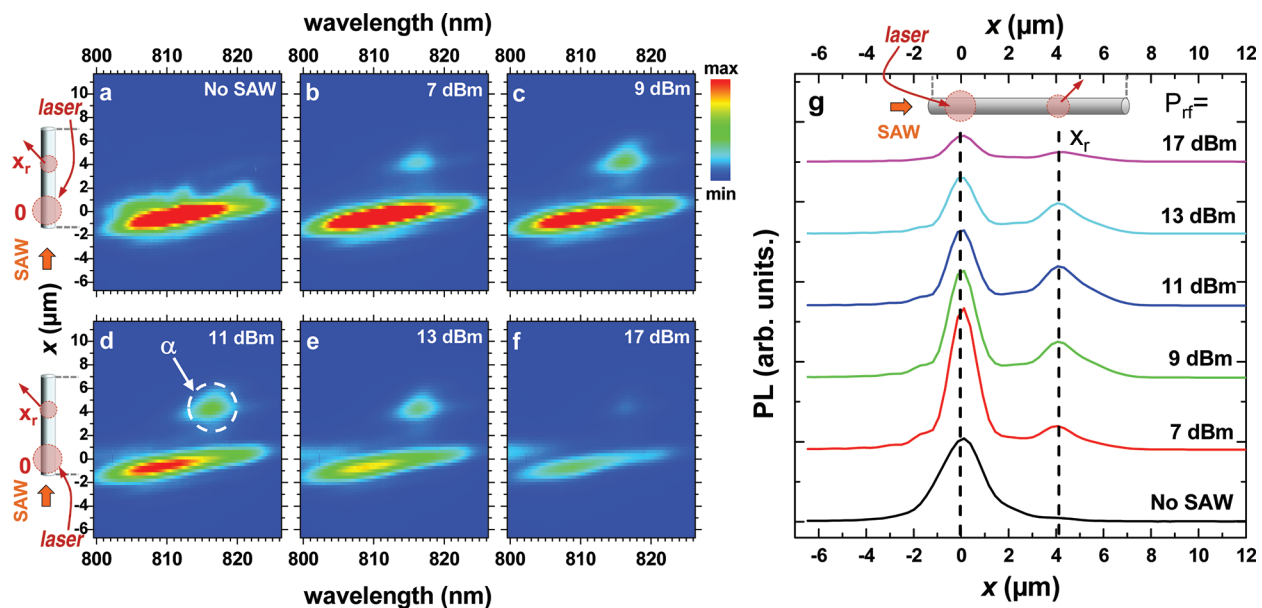


Figure 2. Acoustically induced carrier transport in a nanowire (NW), detected by spatially resolved PL excited by a tightly focused laser beam close to the NW edge facing the acoustic transducer ($x = 0$, cf. diagrams on the left side). (a) For low acoustic powers, emission is restricted to the region close to the excitation spot. (b–e) Moderate acoustic powers induce the transport of electrons and holes to the emission centers at $x_r \approx 4 \mu\text{m}$ (indicated by the dashed line in (g)). (f) Radiative recombination is suppressed at high acoustic powers, leading to the reduction of the PL over the whole NW. (g) Integrated PL along the NW axis (x) for different nominal rf powers applied to the transducer. The dashed circle denoted by α in (d) marks the region selected for the photon autocorrelation measurements of Figure 5.

autocorrelation measurements using a Hanbury–Brown and Twiss (HBT) setup.

The acoustic transport studies were carried out on a 8 μm long NW consisting of an undoped GaAs core of $106 \pm 18 \text{ nm}$

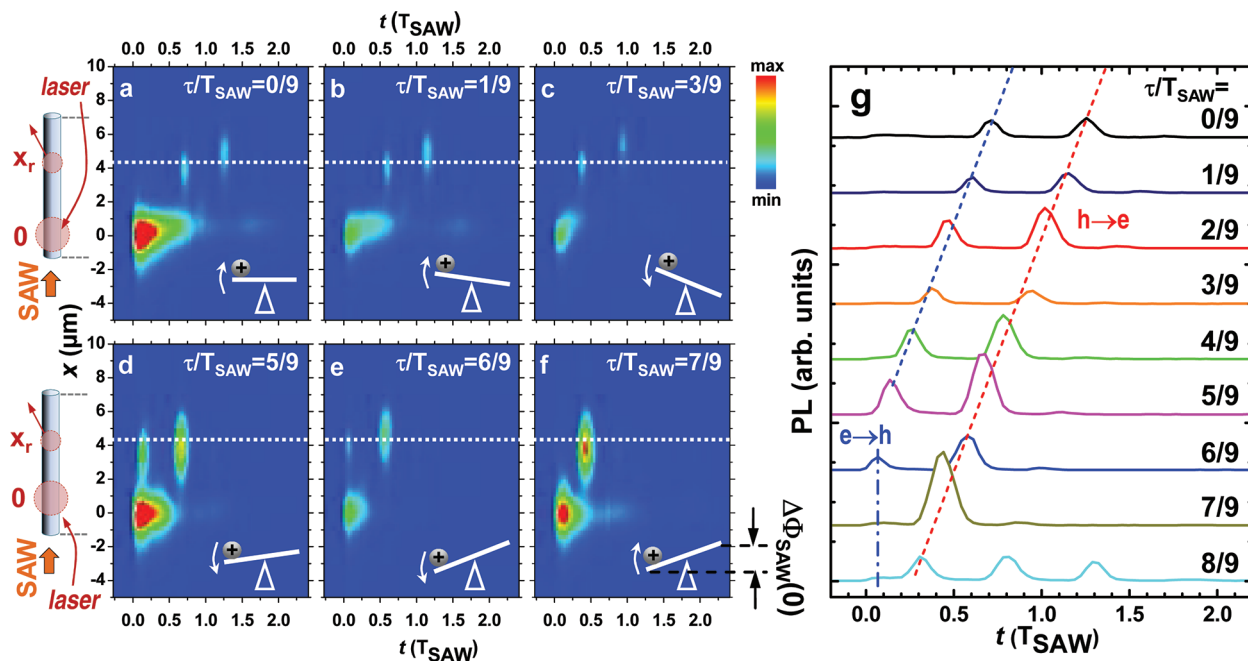


Figure 3. Spatiotemporal photoluminescence (PL) dynamics in the “seesaw”-like potential induced by a surface acoustic wave (SAW). (a–f) PL integrated in the wavelength region from 813.4 to 819 nm as a function of position x along the NW axis (vertical axis) and time delay t (relative to the arrival time of the laser excitation pulse, horizontal scale). The panels were recorded for different excitation phases specified by τ/T_{SAW} (cf. eq 1). According to the simple model described in the text, hole motion is analogous to the slide of a ball on a seesaw whose tilt angle oscillates at the SAW frequency. The piezoelectric potential difference $\Delta\Phi_{\text{SAW}}(t)$ between the generation and recombination sites is proportional to the height difference between the left and right seesaw ends. The insets show the angle and the motion direction (curved arrows) of the seesaw at $t = 0$. All measurements were carried out using a fixed SAW power $P_{\text{rf}} = 11$ dBm. The dotted line indicates the position x_r of the remote recombination centers. (g) PL profiles at x_r (indicated by the dotted lines in (a–f)) for different τ/T_{SAW} ratios.

coated with a 22 ± 9 nm $\text{Al}_x\text{Ga}_{1-x}\text{As}$ shell with x nominally equal to 0.1 (sample A).³ The NWs were grown by molecular beam epitaxy (MBE) using a self-assisted vapor–liquid–solid growth process (see ref 3) on a Si(111) substrate (cf. Figure 1a) and then dispersed on the surface of a SAW delay line consisting of two interdigital transducers deposited by optical lithography on a LiNbO_3 crystal. The use of LiNbO_3 is justified by the fact that, as a strong piezoelectric material, it provides a strong piezoelectric field for the manipulation of carriers in semiconductor structures placed on its surface.^{12,14} The transducers generate SAWs with an acoustic wavelength $\lambda_{\text{SAW}} = 17.5$ μm (cf. Figure 1b, see also Supporting Information, Section A). The corresponding SAW frequency and period are $f_{\text{SAW}} = 226.5$ MHz and $T_{\text{SAW}} = 4.4$ ns, respectively. The optical measurements were carried out on dispersed NWs with the growth axis aligned with the SAW propagation direction. The experiments were performed by mounting the sample in a microscope cryostat for spatially resolved photoluminescence measurements at a nominal temperature of 20 K. A 757 nm diode laser yielding 150 ps wide pulses was used as excitation source. The laser beam was focused onto the NW by using a 50 \times objective. The PL emitted all over the length of the NW was collected by the same objective, imaged on the entrance slit of a spectrometer, and detected with spatial resolution (about 1 μm) by a cooled charge-coupled device (CCD) camera. Figure 1c displays the spectral (horizontal scale) distribution of the PL along the NW axis (vertical scale) recorded under uniform excitation by an expanded laser spot covering the whole NW (cf. left inset). The PL is dominated by emission centers (cf. Figure 1d) that are likely to be induced by band gap modulation along the NW axis due to mixtures of wurzite

and zinc-blende phases in the NWs.^{18–20} The application of a SAW normally leads to a reduction of the PL intensity (dashed lines). This is attributed to the ionization of the photoexcited excitons by the in-plane component F_x of the SAW piezoelectric field followed by the spatial separation of electrons and holes (cf. inset of Figure 1b), thereby reducing the radiative recombination probability. Note that the PL reduction rate is not the same for the different spectral lines, thus indicating different ionization cross-section for the different centers.

The acoustic charge transport was studied by recording PL images excited by a tightly focused laser spot (diameter of approximately 1.5 μm) impinging close to the end of the NW facing the acoustic transducer (i.e., $x = 0$, cf. diagrams on the left side of Figure 2). Figure 2a–f display PL images recorded for increasing acoustic amplitudes [specified in terms of the nominal radio frequency (rf) power P_{rf} applied to the IDT]. In the absence of a SAW, light emission is restricted to the generation site at $x = 0$ with a tail toward positive x values due to carrier diffusion. As the acoustic power increases, emission is observed at a position $x_r = 4$ μm away from the illumination spot, as demonstrated by the PL profiles integrated from 813.4 to 819 nm displayed in Figure 2g. The remote PL, which appears over a wide range of acoustic powers, is attributed to the acoustically induced transport of optically injected electrons and holes to the emission centers close to x_r , followed by their excitonic recombination. For high acoustic powers (Figure 2f), the PL intensity reduces over the whole length of the NW. Under these strong fields, the efficient carrier separation by the SAW field decreases the probability of radiative recombination relative to nonradiative processes. Finally, the highest transport efficiency has been observed for the trap emitting at 816 nm

and not for the one at 835 nm, which has the strongest emission intensity under homogeneous illumination (cf. Figure 1c). This behavior is probably due to the fact that the former is closer and better electrically coupled to the illuminated area of the NW.

From the rf characteristics of the transducers, we determine the threshold amplitude of the piezoelectric field for transport to be $F_x^{(\min)} = 1.8$ kV/cm (see Supporting Information, Section B). The effective carrier mobility is then given by $\mu_{\text{eff}} = \nu_{\text{SAW}}/F_x^{(\min)} = 220$ cm²/(Vs). Note that field amplitudes exceeding $F_x^{(\min)}$ can easily ionize excitons and extract carriers from shallow trapping centers. In fact, if one assumes the energy depth and spatial extension of the trapping centers to be on the order of 10 meV (cf. Figure 1d) and 100 nm, respectively, the corresponding ionization fields will be only 1 kV/cm.

The dynamics of the acoustic transport was investigated by exciting carriers at $x = 0$ using short laser pulses (pulse width $\ll T_{\text{SAW}}$) and following the evolution of the PL along the NW using a gated CCD camera with a gate time of 500 ps. The piezoelectric potential along the NW can be expressed as a function of x and time (t , measured relative to the arrival time of the laser pulse) by

$$\Phi_{\text{SAW}}(x, t) = \Phi_{\text{SAW}0} \sin \left[2\pi \left(\frac{x}{\lambda_{\text{SAW}}} - \left(\frac{t + \tau}{T_{\text{SAW}}} \right) \right) \right] \quad (1)$$

where $\Phi_{\text{SAW}0}$ is the potential amplitude. To follow the PL dynamics under this modulation, the laser pulses were synchronized with the SAW in order to generate carriers at $x = 0$ at well-defined SAW phases specified by the delay τ .²¹ For this purpose, the frequency of the rf signal driving the SAW was divided by a factor of 8 and used to trigger the laser. Laser excitation at different SAW phases $2\pi\tau/T_{\text{SAW}}$ was achieved by electrically delaying the trigger pulses by τ . The panels in Figure 3a–f display spatiotemporal PL maps integrated in the range from 813.4 to 819 nm (cf. Figure 2d) and recorded under a fixed SAW power ($P_{\text{rf}} = 11$ dBm) for different values of τ . As in Figure 2, the time-resolved plots show PL at the illumination site ($x = 0$) as well as close to $x_r = 4$ μm (dotted horizontal lines). The remote PL at x_r appears in form of short light pulses (pulse width comparable to the time resolution of the gated camera) with a repetition rate equal to $T_{\text{SAW}}/2$. This behavior, which is depicted in the time-resolved profiles at x_r displayed in Figure 3g, arises from the oscillatory motion of electrons and holes in the periodic SAW field. Furthermore, the intermittent PL lasts for times exceeding T_{SAW} , which are longer than the PL decay time of 3 ns measured in the absence of acoustic excitation. Finally, the time dependence of the PL varies considerably with the phase delay τ , thus showing that it is very sensitive to the potential profile in the NW at the arrival time of the laser pulse.

In order to reproduce the PL dynamics, we numerically calculated the evolution of the photoexcited density of electrons (n) and holes (p) in the NW by solving the drift/diffusion equations for carrier motion following photoexcitation by a short laser pulse using the procedure delineated in ref 22 (see also Supporting Information, Section C). Carrier trapping at the remote emission centers was modeled by adding to the piezoelectric potential given by eq 1 a local energy minimum at x_r for both electrons and holes. Under these conditions, the remote PL dynamics is governed by the acoustic transport of

both electrons and holes along the NW as this potential oscillates with the SAW frequency. We show in the Supporting Information that essentially all the experimental features of Figure 3g are well reproduced by the simulations.

Since the separation between the illumination spot and the remote recombination centers is shorter than $\lambda_{\text{SAW}}/4$, a simple physical picture for the carrier dynamics in Figure 3, consistent with the simulation results, is obtained by assuming a linear potential variation between these two positions. Under these conditions, hole motion becomes analogous to the slide of a ball on an oscillating seesaw whose difference of end-point heights is proportional to the potential difference $\Delta\Phi_{\text{SAW}}(t) = \Phi_{\text{SAW}}(0, t) - \Phi_{\text{SAW}}(x_r, t)$, as indicated by the insets of Figure 3a–f. The diagrams show the angular position and motion direction of the seesaw at the laser excitation time $t = 0$. Electrons, in contrast, move toward the locations of higher potential. The remote recombination requires that a fraction of the carriers reaching the remote emission center remains trapped until the arrival of carriers of the opposite polarity in a subsequent SAW half-cycle. For $0 < T_{\text{SAW}} \leq 4/9$, $\Delta\Phi_{\text{SAW}}(0)$ is positive, leading to the transfer and subsequent trapping of holes at the remote site. Remote recombination occurs when $\Delta\Phi_{\text{SAW}}(t)$ changes sign and drives electrons to x_r , giving rise to the first PL pulse in Figure 3a–c (labeled by $e \rightarrow h$ in Figure 3g). Note, however, that not all holes recombine, since some of them are driven back to $x = 0$ when the $\Delta\Phi_{\text{SAW}}(t)$ becomes negative. The second remote PL pulse in Figure 3a–c appears half a SAW cycle later, when these holes return to x_r and recombine with electrons that remain in the trap ($h \rightarrow e$ pulses in Figure 3g). Note that these ($h \rightarrow e$ pulses) are stronger than the first ($e \rightarrow h$ pulses) ones. This effect is probably due to the fact that electrons can be more efficiently transferred and trapped at the remote recombination centers than holes. Depending on the excitation conditions, this process can repeat many times leading to the emission of additional light pulses.

The PL dynamics for $5/9 \leq \tau/T_{\text{SAW}} < 1$ (Figure 3d–f) can be qualitatively understood by simply exchanging the roles of electrons and holes. In this case, $\Delta\Phi_{\text{SAW}}(0) < 0$ pushes electrons toward the traps at x_r . The first remote PL pulse is expected when holes are transported to x_r in a subsequent SAW half-cycle ($h \rightarrow e$ pulses in Figure 3g). In the experiments, however, the $h \rightarrow e$ pulses are preceded by the pulses arriving at short delays indicated by the dash-dotted vertical lines in Figure 3g. We show in the Supporting Information that these pulses are well-reproduced in simulations performed assuming that the electrons transported by the SAW recombine with holes present at x_r prior to the arrival of the laser pulse. These holes do not originate from photoexcitation during a previous laser cycle, since under the used excitation conditions the remote PL vanishes within times much shorter than the laser repetition rate of 35.3 ns. They are probably induced by the ionization of shallow acceptors in the NW and subsequent capture in the remote traps near x_r .

The pumping of quantum dots (QDs) by the alternating trains of electrons and holes generated by a SAW has been proposed by Wiele and co-workers as a process for the realization of high-frequency turnstile single-photon sources.²³ More recently, Couto et al.¹⁷ have demonstrated an antibunched photon source based on the acoustic pumping of a QD ensemble in quasi-planar GaAs structures. In these experiments, the tunable SAW fields not only transport carriers to the ensemble but also restricts the emission to a few centers

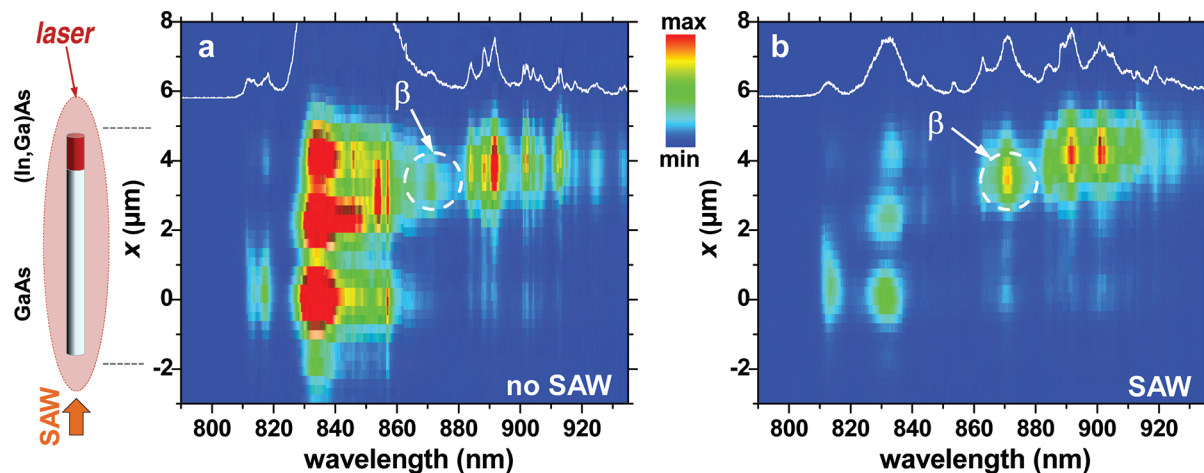


Figure 4. Acoustic transport in GaAs/(In,Ga)As NWs. (a) Spectrally resolved PL map along the NW axis recorded under illumination of the whole NW (left inset) in the absence of a SAW. (b) Corresponding PL map under a SAW generated using $P_{\text{rf}} = 9$ dBm, which leads to enhanced emission from the (In,Ga)As segment due to acoustic transport. The superimposed curves are integrated PL profiles in the (In,Ga)As segment. The dashed circle β marks the region selected for the photon autocorrelation measurements of Figure 5.

within it, thereby leading to the emission of antibunched photons.

Similarly, the acoustic transport in NWs opens the way for the realization of high-frequency single-photon emitters, which profit from the high light extraction efficiency associated with the NW geometry. In order to demonstrate the potentials of this approach, we have introduced QD-like recombination centers in the NW by exposing the growing surfaces to In and As fluxes during the last steps of the MBE deposition of the GaAs core (sample B). This procedure lead to the formation of a short (approximately 300 nm long) segment containing In inclusions (denoted here as the (In,Ga)As segment). Because of the modified MBE growth conditions, the (In,Ga)As segments have a larger diameter (200 nm) as well as a higher density of planar defects compared to sample A, as confirmed by transmission electron microscopy (TEM). The average length of the NWs in this sample is 7 μm . Figure 4a displays a spatially resolved PL micrograph of sample B excited by an expanded laser beam. The strongest PL lines, which appear for wavelengths shorter than 840 nm, are similar to the ones observed for sample A (cf. Figure 1c). Sample B exhibits, in addition, a series of narrow emission lines at wavelengths extending from 860 up to 930 nm, which are absent in Figure 1c. These lines are attributed to localized recombination centers associated with In incorporation within the (In,Ga)As segment. It is interesting to note that these narrow lines are also observed in the GaAs segment of sample B but with a much lower intensity. The formation of a thin (In,Ga)As layer on the GaAs sidewalls during the growth of the (In,Ga)As section, which could account for the presence of (In,Ga)As lines in the GaAs segment, has recently been reported.²⁴ However, the fact that the narrow lines in the GaAs segment have almost the same spectral shape as in the (In,Ga)As one indicates that they rather stem from the guiding of the PL from the (In,Ga)As segment through the GaAs section, which is transparent in this wavelength region.

The effects of the SAW fields on the PL of sample B are illustrated in Figure 4b. In this case, SAWs with an acoustic wavelength and frequency of $\lambda_{\text{SAW}} = 11.67$ μm and $f_{\text{SAW}} = 338$ MHz, respectively, were used. The acoustic modulation broadens the emission lines and reduces the overall PL

intensity. Note, however, that the PL quenching is more pronounced for the lines at short wavelength associated with GaAs. This behavior is attributed to the higher exciton ionization probability for these emission centers. The resulting electrons and holes are then acoustically transported to the (In,Ga)As section, where they recombine. Finally, the rf-power dependence of the lines at longer wavelengths detected on the GaAs segment follows closely the one of the (In,Ga)As segment, in agreement with the light guiding mechanism described above.

Investigations of the photon emission statistics in samples A and B were carried out by photoexciting carriers using light pulses focused on the GaAs side of the NWs (close to the end facing the IDT), as illustrated in the right insets of Figure 5. The PL induced by the recombination of carriers acoustically transported to the opposite end of the NW was spectrally filtered and analyzed using a HBT setup consisting of two Si avalanche photodetectors, each placed at one of the two output ports of a 50/50 nonpolarizing beam splitter.²⁵ The photodetectors were connected to either the “start” or “stop” inputs of a time-correlated single photon counting electronics which delivers a histogram of the temporal distribution of coincidences of the two photodetectors. When triggered by the laser pulses, the same setup also yields time-resolved PL traces. The emission centers selected for analysis were those centered at 816 and 870 nm for samples A and B, respectively (corresponding to the region indicated by the dashed circles in Figure 2d and Figure 4, respectively). In the case of sample B, the center at 870 nm was selected because it is the one displaying the strongest PL under remote excitation, as illustrated in Figure S5 (Supporting Information). In addition, this line is spectrally well-separated from other emission centers, thus making its selection easier using band-pass filters. The curves marked as α and β in Figure 5a compare time-resolved traces of samples A and B, respectively, recorded under these conditions. The recombination pulses in sample B persist over times much longer than for sample A. This behavior may be associated with a higher density of trapping centers, which hampers the transport efficiency. The α and β traces in Figure 5b,c display the corresponding autocorrelation histograms. We have also included in Figure 5c a coincidence

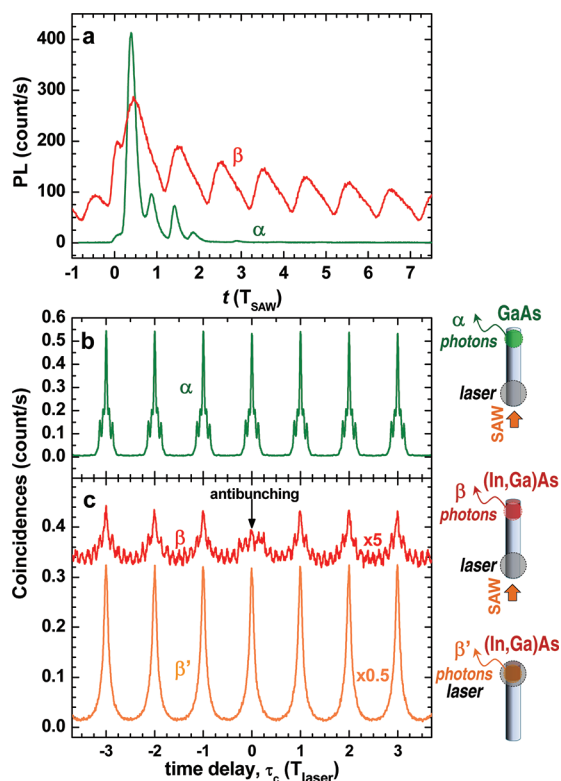


Figure 5. Photon autocorrelation measurements in NWs. (a) Time-resolved PL at the remote recombination site of a GaAs NW (sample A, α curve) and a GaAs NW with an (In,Ga)As segment (sample B, β curve). The right insets display the excitation configurations α , β , and β' for the autocorrelation measurements. The PL detection regions for samples A and B are indicated by the dashed circles in Figure 2d and Figure 4, respectively. Autocorrelation measurement of (b) sample A under remote excitation (configuration α) and (c) sample B under remote (configuration β) and local excitation (configuration β'). The latter was recorded without a SAW with the laser spot focused on the (In,Ga)As segment. The laser repetition periods were 35.3 and 23.6 ns for samples A and B, respectively. The laser intensities were 2 μ W for curves α and β and 0.6 μ W for β' .

histogram recorded for sample B without a SAW with the laser spot positioned directly on the (In,Ga)As segment (trace β'). Because of the synchronization of the laser and SAW periods, the histograms exhibit two periodicities: a short one associated with the SAW period (T_{SAW}) and a longer one determined by the laser repetition rate $T_{\text{laser}} = 8T_{\text{SAW}}$. Traces α and β' are periodic over the whole range of delays; their shape can be reproduced by the numeric autocorrelation of the corresponding time-resolved spectra. The emission involves, therefore, contributions from many quantum centers. Histogram β , in contrast, shows a clear reduction in the coincidence rate at an autocorrelation delay $\tau_c = 0$ (photon antibunching), thereby attesting to the nonclassical behavior of the emission centers. Finally, the fact that antibunching has not been observed for excitation directly on the (In,Ga)As area points to the essential role of the acoustic transport for antibunched photon emission from the QD ensemble. The latter is further supported by the dependence of the autocorrelation histograms on acoustic power presented in the Supporting Information (Section D).

From the reduction $r_c = 10\%$ of the coincidence rate at $\tau_c = 0$ in Figure 5b (trace β), we estimate that $1/r_c = 10$ quantum emission centers are present in the detection area.²⁵ This number is still too high for applications in single-photon

sources. Although it can be reduced by diminishing the size of the collection area or the spectral collection bandwidth, the most promising approach would certainly be the optimization of the growth conditions to create a single (In,Ga)As QD within the NW.

In conclusion, we have demonstrated the oscillatory motion of electrons and holes in undoped GaAs NWs under the high-frequency piezoelectric field of a SAW. The results presented here open the way for the contactless control of the electro-optical properties of NWs with subnanosecond time resolution. As an example of application, we presented a source of antibunched photon pulses at high repetition rates based on the acoustically induced charge pumping of QD states embedded in the NW. Further optimization of these structures will provide efficient single-photon sources at gigahertz repetition rates and high light extraction efficiency, a necessary combination for achieving high bit rates in quantum cryptography. Finally, the piezoelectric field of a Rayleigh SAW also possesses a vertical component, which can drive carriers in vertical NWs grown epitaxially on piezoelectric substrates (such as those grown on III–V semiconductors). The combination of this vertical motion with the well-established acoustic carrier transport in planar semiconductor structures would provide a powerful framework for devices based on the high-frequency charge transfer between planar semiconductor structures and electrically interconnected NWs grown epitaxially on them.

■ ASSOCIATED CONTENT

Supporting Information

Details about the amplitude of the piezoelectric field and dependence of the transport efficiency on rf frequency and power. Details of the simulations of acoustic transport in nanowires and complementary experimental results on photon-antibunching in GaAs/(In,Ga)As nanowires. This material is available free of charge via the Internet at <http://pubs.acs.org>.

■ AUTHOR INFORMATION

Corresponding Author

*E-mail: alberto@pdi-berlin.de.

■ ACKNOWLEDGMENTS

We thank M. Ramsteiner for discussions and A. Trampert for the TEM investigations. We also acknowledge the expertise of C. Herrmann, S. Krauß, and W. Seidel in the preparation of the SAW samples. A. H.-M. thanks the support of the “Comissionat per a Universitats i Recerca del Departament d’Innovació, Universitats i Empresa de la Generalitat de Catalunya”. M.M., M.M.L.J., A. G.-C., and A. C. thank the Spanish Ministry of Science and Innovation (grant Nos. TEC2009-12075 and MAT2009-10350) for financial support. We also acknowledge the financial support from the German DFG (grant GE 2224/2).

■ REFERENCES

- (1) Lieber, C. M.; Wang, Z. L. *MRS Bull.* **2007**, 32, 99.
- (2) Yang, P.; Yan, R.; Fardy, M. *Nano Lett.* **2010**, 10, 1529–1536.
- (3) Breuer, S.; Pfüller, C.; Flissikowski, T.; Brandt, O.; Grah, H. T.; Geelhaar, L.; Riechert, H. *Nano Lett.* **2011**, 11, 1276–1279.
- (4) Rocke, C.; Zimmermann, S.; Wixforth, A.; Kotthaus, J. P.; Böhm, G.; Weimann, G. *Phys. Rev. Lett.* **1997**, 78, 4099.
- (5) Shilton, J. M.; Talyanskii, V. I.; Pepper, M.; Ritchie, D. A.; Frost, J. E. F.; Ford, C. J. B.; Smith, C. G.; Jones, G. A. C. *J. Phys.: Condens. Matter* **1996**, 8, L531.

- (6) Stotz, J. A. H.; Hey, R.; Santos, P. V.; Ploog, K. H. *Nat. Mater.* **2005**, *4*, 585.
- (7) Couto, O. D. D. Jr.; Iikawa, F.; Rudolph, J.; Hey, R.; Santos, P. V. *Phys. Rev. Lett.* **2007**, *98*, 036603.
- (8) Hernández-Mínguez, A.; Biermann, K.; Lazić, S.; Hey, R.; Santos, P. V. *Appl. Phys. Lett.* **2010**, *97*, 242110.
- (9) Ebbecke, J.; Strobl, C.; Wixforth, A. *Phys. Rev. B* **2004**, *70*, 233401.
- (10) Leek, P. J.; Buitelaar, M. R.; Talyanskii, V. I.; Smith, C. G.; Anderson, D.; Jones, G. A. C.; Wei, J.; Cobden, D. H. *Phys. Rev. Lett.* **2005**, *95*, 256802.
- (11) Buitelaar, M. R.; Kashcheyevs, V.; Leek, P. J.; Talyanskii, V. I.; Smith, C. G.; Anderson, D.; Jones, G. A. C.; Wei, J.; Cobden, D. H. *Phys. Rev. Lett.* **2008**, *101*, 126803.
- (12) Ebbecke, J.; Maisch, S.; Wixforth, A.; Calarco, R.; Meijers, R.; Marso, M.; Lüth, H. *Nanotechnology* **2008**, *19*, 275708.
- (13) Völkl, S.; Schülein, F. J. R.; Knall, F.; Reuter, D.; Wieck, A. D.; Truong, T. A.; Kim, H.; Petroff, P. M.; Wixforth, A.; Krenner, H. J. *Nano Lett.* **2010**, *10*, 3399–3407.
- (14) Kinzel, J. B.; Rudolph, D.; Bichler, M.; Abstreiter, G.; Finley, J. J.; Koblmüller, G.; Wixforth, A.; Krenner, H. J. *Nano Lett.* **2011**, *11*, 1512–1517.
- (15) Parkinson, P.; Lloyd-Hughes, J.; Gao, Q.; Tan, H. H.; Jagadish, C.; Johnston, M. B.; Herz, L. M. *Nano Lett.* **2007**, *7*, 2162–2165.
- (16) Claudon, J.; Bleuse, J.; Malik, N. S.; Bazin, M.; Jaffrennou, P.; Gregersen, N.; Sauvan, C.; Lalanne, P.; Gérard, J.-M. *Nat. Photonics* **2010**, *4*, 174.
- (17) Couto, O. D. D. Jr.; Lazić, S.; Iikawa, F.; Stotz, J.; Hey, R.; Santos, P. V. *Nat. Photonics* **2009**, *3*, 645.
- (18) Ba Hoang, T.; Moses, A. F.; Ahtapodov, L.; Zhou, H.; Dheeraj, D. L.; van Helvoort, A. T. J.; Fimland, B.-O.; Weman, H. *Nano Lett.* **2010**, *10*, 2927–2933.
- (19) Jancu, J.-M.; Gauthron, K.; Largeau, L.; Patriarche, G.; Harmand, J.-C.; Voisin, P. *Appl. Phys. Lett.* **2010**, *97*, 041910.
- (20) Spirkoska, D.; et al. *Phys. Rev. B* **2009**, *80*, 245325.
- (21) In the present experiments, the absolute SAW phase at $t = 0$ (and, therefore, τ) depends on the NW location on the delay line and cannot be directly determined. These values were determined from the simulations of the PL dynamics.
- (22) García-Cristóbal, A.; Cantarero, A.; Alsina, F.; Santos, P. V. *Phys. Rev. B* **2004**, *69*, 205301.
- (23) Wiele, C.; Haake, F.; Rocke, C.; Wixforth, A. *Phys. Rev. A* **1998**, *58*, R2680.
- (24) Messing, M. E.; Wong-Leung, J.; Zanolli, Z.; Joyce, H. J.; Tan, H. H.; Gao, Q.; Wallenberg, L. R.; Johansson, J.; Jagadish, C. *Nano Lett.* **2011**, *11*, 3899–3905.
- (25) Lounis, B.; Orrit, M. *Rep. Prog. Phys.* **2005**, *68*, 1129–1179.